ADVANCED FUNCTIONAL MATERIALS
www.afm-journal.de

Fast Ion Transport in Li-Rich Alloy Anode for High-Energy-Density All Solid-State Lithium Metal Batteries

Xuejie Gao, Xiaofei Yang, Ming Jiang, Matthew Zheng, Yang Zhao, Ruying Li, Wenfeng Ren, Huan Huang, Runcang Sun, Jiantao Wang, Chandra Veer Singh,* and Xueliang Sun**

All-solid-state Li batteries (ASSLBs) with solid-polymer electrolytes are considered promising battery systems to achieve improved safety and high energy density. However, Li dendrite formation at the Li anode under high charging current density/capacity has limited their development. To tackle the issue, Li-metal alloying has been proposed as an alternative strategy to suppress Li dendrite growth in ASSLBs. One drawback of alloying is the relatively lower operating cell voltages, which will inevitably lower energy density compared to cells with pure Li anode. Herein, a Li-rich $Li_{13}In_3$ alloy electrode (LiRLIA) is proposed, where the $Li_{13}In_3$ alloy scaffold guides Li nucleation and hinders Li dendrite formation. Meanwhile, the free Li can recover Li's potential and facilitate fast charge transfer kinetics to realize high-energy-density ASSLBs. Benefitting from the stronger adsorption energy and lower diffusion energy barrier of Li on a $Li_{13}In_3$ substrate, Li prefers to deposit in the 3D $Li_{13}In_3$ scaffold selectively. Therefore, the Li–Li symmetric cell constructed with LiRLIA can operate at a high current density/capacity of 5 mA cm^{-2}/5 mAh cm^{-2} for almost 1000 h.

1. Introduction

The pursuit of high-energy-density and high-safety energy storage devices to fit the demand of electric vehicles and portable electronic devices have revived the development of ASSLBs.[1] The use of non-flammable solid-state electrolytes (SSEs) makes it possible to switch the anode material from graphite, as used in the state-of-the-art of Li-ion batteries, with metallic lithium, which can remarkably enhance energy density and safety.[2] Among various SSE systems, solid-polymer electrolytes (SPEs) have attracted special interest for practical application due to their high flexibility, high chemical/electrochemical stability, low cost, and scalable fabrication process.[3] However, uncontrollable Li dendrite growth[4] and poor mechanical strength[5] of SPEs result in interior short-circuiting and dramatically limited cycling life and rate capability of SPE-based ASSLBs.[6]

To tackle this concern, tremendous efforts have been devoted to developing functional inorganic fillers,[7] designing cross-linking structures[8] as well as exploring novel electrolyte additives to assist suppress Li dendrites.[9] The former two strategies aim to enhance the mechanical strength of SPEs. For instance, the introduction of Garnet-type $Li_{6.75}La_3Zr_{1.75}Ta_{0.25}O_{12}$ (LLZTO) with an ultra-high shear modulus of 55 GPa into the poly(ethylene oxide)[10] realized stable Li plating/stripping in for over 400 h at 0.1 mA cm^{-2}. The latter plays an important role in regulating Li deposition kinetics and promoting uniform Li deposition. Our group extended the cycling life of Li–Li symmetric cells by one order of magnitude at a current density of 0.2 mA cm^{-2} (capacity: 0.2 mAh cm^{-2}) with the introduction of a Cs^+ additive,[11] which facilitates the

X. Gao, X. Yang, M. Zheng, Y. Zhao, R. Li, X. Sun
Department of Mechanical and Materials Engineering
University of Western Ontario
London, Ontario N6A 5B9, Canada
E-mail: xsun9@uwo.ca

X. Gao, W. Ren, R. Sun
Liaoning Key Laboratory of Lignocellulosic Chemistry and Biomaterials
College of Light Industry and Chemical Engineering
Dalian Polytechnic University
Dalian 116034, China

M. Jiang
Institute of Physical Science and Information Technology
Anhui University
Hefei 230601, China

The ORCID identification number(s) for the author(s) of this article can be found under https://doi.org/10.1002/adfm.202209715.

M. Jiang, C. V. Singh
Department of Materials Science and Engineering
University of Toronto
184 College Street, Suite 140, Toronto, Ontario M5S 3E4, Canada
E-mail: chandraveer.singh@utoronto.ca

H. Huang, J. Wang
Glabat Solid-State Battery Inc.
700 Collip Circle, London, Ontario N6G 4X8, Canada
E-mail: wangjt@glabat.com

J. Wang
China Automotive Battery Research Institute
Beijing 100088, P. R. China

C. V. Singh
Department of Mechanical and Industrial Engineering
University of Toronto
5 King's College Road, Toronto, Ontario M5S 3G8, Canada

DOI: 10.1002/adfm.202209715

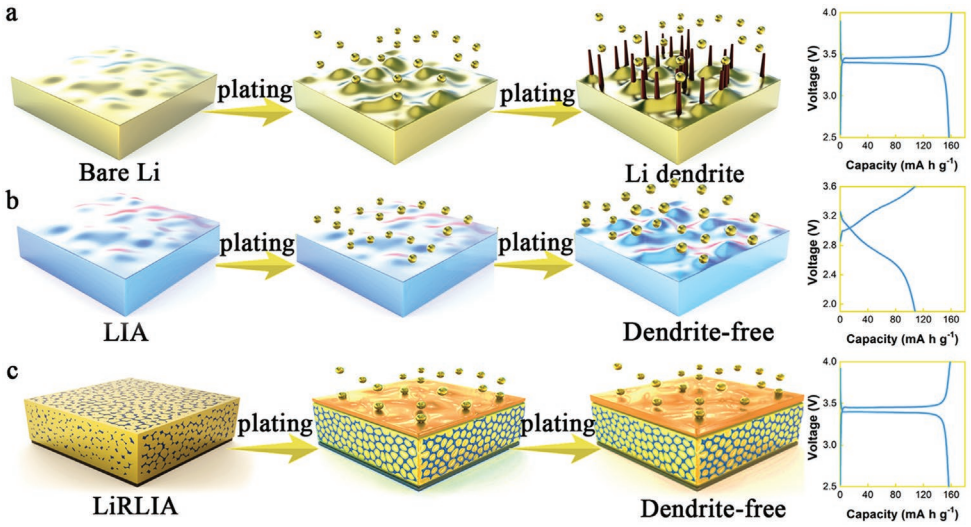

Figure 1. Schematic illustration of Li plating process in SPE-based Li metal batteries with a) bare Li, b) LIA, and c) LiRLIA.

formation of a self-healing electrostatic shield to enable uniform Li deposition. Despite the great progress, the low operating current densities, and areal capacities (typically less than 0.5 mA cm^{-2} and 0.5 mAh cm^{-2}) based on 2D Li foils are still far away from meeting the requirements of ASSLBs in practical application.[12] In other words, at moderate current densities the conductivity inhomogeneity promotes selective electrod deposition on sparse local sites where mossy dendrites can proliferate.

Alternatively, Li-metal alloys, where the Li component is stored in an ionic form rather than a metallic form, have been chosen as anodes in ASSLBs to resist Li dendrite growth,[13] even under harsh operating conditions of over 5 mA cm^{-2}/5 mAh cm^{-2}. A drawback is the relatively lower operating potentials of Li-metal alloys inevitably lowers energy density.[14] Herein, to recover Li's potential, while preserving the Li dendrite suppression capability more Li is introduced into a totally alloyed Li-metal alloy to form a Li-rich alloy anode (LiRLIA). As illustrated in **Figure 1**a, for the bare Li, due to the uneven Li deposition, the Li dendrite can easily penetrate the soft SPE and seriously result in internal short-circuiting. The situation will be worse under higher operating current densities or high areal capacities because of more serious Li dendrite growth. Compared with bare Li, pure Li-metal alloy (named as LIA), possesses a strong capability in suppressing Li dendrite growth by storing Li ions in ionic form (Figure 1b). Herein we chose the Li-In alloy as the representative LIA. The main drawback is the relatively low potential of 0.6 V versus Li^+/Li, which reduces energy density. To prevent the Li dendrite growth on bare Li surface as well as recover the potential of Li-In alloy to the level of Li, a Li-rich Li-In alloy (LiRLIA) anode is developed in this work. As illustrated in Figure 1c, the Li-In alloy ($Li_{13}In_3$) acts as a 3D scaffold for Li accommodation as well as alleviating the volume change, while the residue Li acts as the Li source and transports between anode and cathode during the charging/discharging process. Benefitting from the stronger adsorption energy and lower diffusion energy barrier of Li on $Li_{13}In_3$ substrate, Li prefers to selectively and smoothly deposit in the 3D $Li_{13}In_3$ scaffold, thus avoiding Li dendrite growth. More importantly, the residual Li in the 3D $Li_{13}In_3$ scaffold recovers the potential of Li-In alloy to Li's level, attributing to higher energy density output. As a result, the assembled Li–Li symmetric cells using LiRLIA stably run at high current densities and areal capacities of over 5 mA cm^{-2} and 5 mAh cm^{-2}, which are over one of magnitude higher than most previous SPE-based cells. Moreover, under a current density/capacity of 0.5 mA cm^{-2}/1 mAh cm^{-2}, the cell demonstrates ultra-long cycling life of over 6800 h. The strong Li dendrite capability of the LiRLIA anode enables the Li-LFP full cell with excellent rate capability and cycling performance, which are 100 mAh g^{-1} output at 10 C and over 83% capacity retention at 5 C for 2000 cycles. The fast ion transport in anode side is beneficial for the high-capacity, dendrite-free battery cycling in both symmetric cells and in full cells. This work will open a new window to design high-performance anode for high-power-density and high-energy-density ASSLBs.

2. Result and Discussion

LiRLIA electrode in this work is fabricated by Li-rich $Li_{13}In_3$ alloy (LiRLIA) infusion into a vertically aligned ZnO@CNT template which is constructed by a freeze-drying method. Based on the anisotropic crystal growth, the lamellar ice inside this template can act as an in situ formed template and transform the ZnO@CNT into a vertically aligned structure with numerous vertically aligned micro-walls[11,15] (thickness: ≈12 µm, distance: ≈35 µm, Figure S1, Supporting Information). For the template design, ZnO nanoparticles are uniformly coated on the surface of carbon nanotube (CNT) by using an atomic layer deposition (ALD) method.[16] Because of the lithiophilic property of coated ZnO, the Li-rich metal alloy infusion process is easy and energetically favorable. As shown in Figure S2, Supporting Information, there is a strong affinity to the template, and the LiRLIA electrode is completely infused with molten Li-rich metal alloy after about 40 s. This infusion process is similar to our previous work for the design of the VA-Li electrodes.[17] The

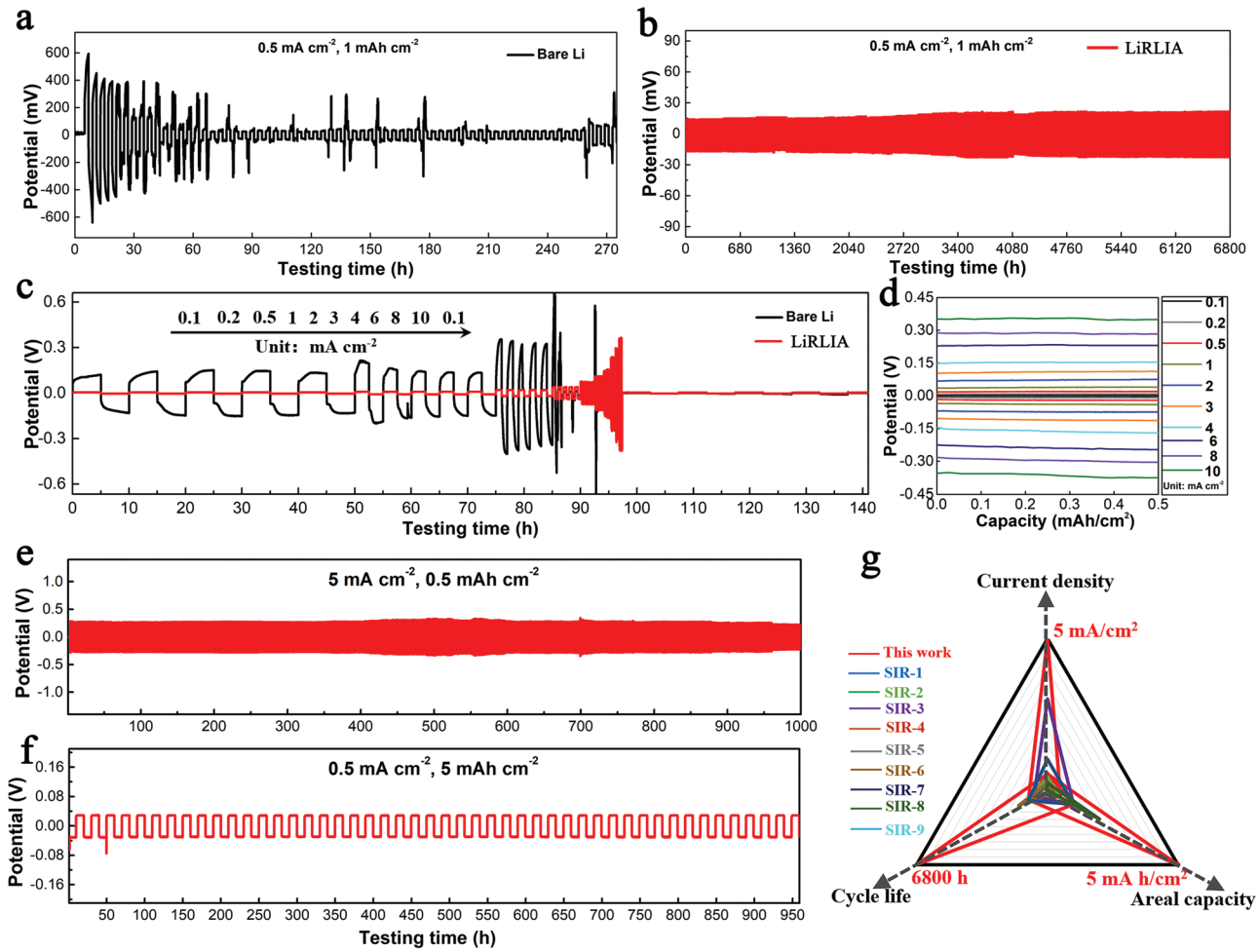

Figure 2. Cycling stability of bare Li and LiRLIA symmetric cells with SPEs. a,b) Bare Li and LiRLIA symmetric cells cycled at a current density of 0.5 mA cm^{-2} and 1 mAh cm^{-2}. c) Rate performance of both symmetric cells from 0.1 to 10 mA cm^{-2}. d) Charge and discharge profiles of LiRLIA symmetric cells at a different rate. e) 5 mA cm^{-2}, 0.5 mAh cm^{-2} and f) 0.5 mA cm^{-2}, 5 mAh cm^{-2}. g) Comparison of this work with other lithium symmetric cells with SPE from literature.

morphology of the LiRLIA electrode at the micro-level is characterized by SEM, as shown in Figure S3, Supporting Information. From the top view, the microstructure is different from the vertically aligned template, suggesting a successful Li-rich metal alloy infusion process. The cross-sectional view of SEM also confirms the thickness of the LiRLIA is around 250 µm. In addition, the XRD pattern of the LiRLIA electrode as shown in Figure S4, Supporting Information, demonstrates the metal alloy is $Li_{13}In_3$.

To demonstrate the Li plating/stripping behavior and electrochemical performance of the LiRLIA electrode, Li–Li symmetrical cells with SPE are studied, where bare Li is selected for comparison. As shown in **Figure 2**, displays the Li deposition behavior in the symmetric cells and relevant symmetric cell performance using designed LiRLIA electrode and bare Li as counterparts. Figure 2a first demonstrates the bare Li symmetric cell performance at a current density of 0.5 mA cm^{-2} (capacity: 1 mAh cm^{-2}). It has a large overpotential of around 600 mV at the beginning cycle. Subsequently, there is a large fluctuation in the plating/stripping profiles after 30 h and the overpotential suddenly drops to nearly 0 V after 90 h, indicating short-circuiting. Compared with a bare Li symmetric cell, the LiRLIA symmetric cell can deliver a different performance because the $Li_{13}In_3$ alloy acts as a 3D scaffold for Li accommodation and alleviates the anodic volume change, while the residual Li acts as the Li source and transports Li^+ between anode and cathode during the plating/stripping process. For instance, as shown in Figure 2b, the Li symmetric cell assembled with LiRLIA electrode exhibits lower overpotential than that of bare Li at the same current density and capacity (0.5 mA cm^{-2}, 1 mAh cm^{-2}). Even after 6800 h, the overpotential of the LiRLIA symmetric cell is able to maintain its cycling stability, just around 20 mV with negligible change. This lower overpotential and dendrite-free capability compared with bare Li can be attributed to the 3D structure design of LiRLIA which can reduce the local current density because of its high surface area and leverage its high lithiophilicity to offer preferential Li nucleation sites. Hence, replated Li atoms can be filled into the interior porosity of the LiRLIA electrode instead of aggregated on the surface during plating/striping

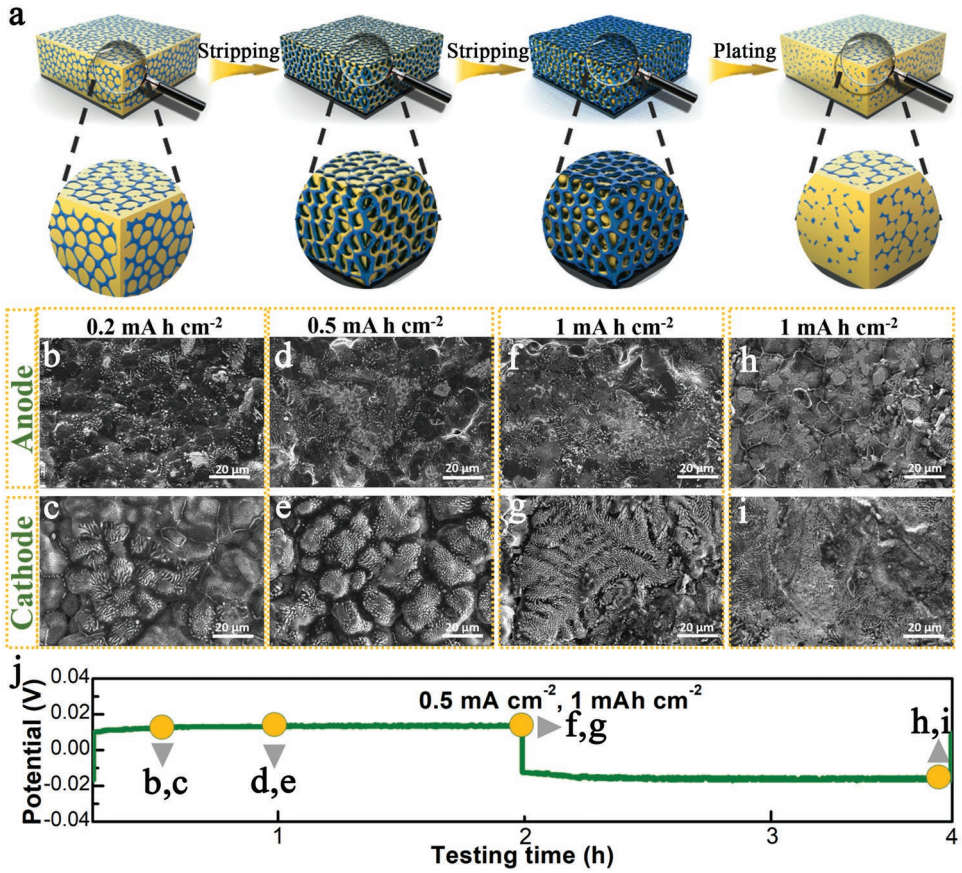

Figure 3. a) Schematic illustration of the lithium stripping/plating process of LiRLIA, corresponding well with SEM images of surface morphology evolution, from the capacities of 0.2 mAh cm^{-2} to 1 mAh cm^{-2} at a current density of 0.5 mA cm^{-2}. SEM images of surface morphology evolution of LiRLIA anode/cathode after b,c) 0.2 mAh cm^{-2}, d,e) 0.5 mAh cm^{-2}, f,g) 1 mAh cm^{-2} of Li stripping, and h,i) 1 mAh cm^{-2} of Li plating at a current density 0.5 mA cm^{-2}. j) The voltage profile indicated the Li plating and stripping states at a current density of 0.5 mA cm^{-2}, corresponding to (b)–(i).

process. Moreover, the different rate performance of Li symmetric cell assembled with LiRLIA and bare Li as counterparts from 0.1 to 10 mA cm^{-2} is also tested to further confirm the LiRLIA capability in Li dendrite suppression. As shown in Figure 2c, the LiRLIA symmetric cell displays a lower overpotential than that of a bare Li symmetric cell at different current densities, which can be attributed to the large surface area provided by LiRLIA that reduces local current density. It shows a stable and reversible plating/stripping behavior, even at an ultrahigh current density of 10 mA cm^{-2} with a relatively low overpotential around 350 mV. The corresponding detailed voltage profile is shown in Figure 2d. When applying a higher current density from 0.1 to 10 mA cm^{-2}, the voltage increases to a stable platform at ≈350 mV, coinciding well with the different current density curves mentioned above. On the contrary, the occurrence of short-circuits is observed in the bare Li symmetric cell when the current density just increases to 1 mA cm^{-2}, which can be attributed to the non-uniform Li deposition and serious Li dendrite growth at a high current density. More importantly, when the cell returns to the current density of 0.1 mA cm^{-2}, the overpotential can fully reverse to the original overpotential, just about 6 mV, indicating high reversibility of the LiRLIA electrode.

It is well known that the cycling life, operating current density, and capacity can play a significant role in the design and development of high energy/power density ASSLB. Therefore, the Li dendrite suppression capability of the LiRLIA electrode is further studied at an elevated current density of 5 mA cm^{-2} and capacity of 5 mAh cm^{-2}, as shown in Figure 2e,f. Interestingly, the LiRLIA electrode can realize stable plating/stripping performance at both a higher current density/areal capacity for 1000 h (5 mA cm^{-2}, 0.5 mAh cm^{-2}) and 950 h (0.5 mA cm^{-2}, 5 mAh cm^{-2}), **Figure 3**e and Figure 2f, respectively. The respective overpotential is ≈300 mV (Figures S6 and S7, Supporting Information) and 30 mV (Figure S8, Supporting Information). There is no doubt that such excellent performance of Li symmetric cell-based SPE is superior to recent publications in terms of operating current density, areal capacity, and cycle life listed in Figure 2g and Table S1, Supporting Information. While, the Li symmetric results also demonstrates an excellent operating current density and capacity when compares with other Li metal alloy anode for solid-state batteries (Figure S9, Supporting Information). Overall, the as-designed LiRLIA demonstrated excellent Li dendrite suppression under high operating current densities as well as ultralong cycle life, which are over one of magnitude higher than most previous

SPE-based cells. Hence, we believe this work can pave the way for the development of future 3D Li/LiIn alloy anode-based ASSLBs.

In terms of the Li symmetric cell results, the stripping and plating process of LiRLIA is illustrated as schematic diagrams in Figure 3a. During the stripping process, Li ions prefer to strip selectively from the 3D LiRLIA electrode, while the $Li_{13}In_3$ framework can still maintain a 3D structure within the high surface area and adequate inner space. With the increase of the areal capacity at the same current density, the free Li can still strip from the electrode, as well 3D $Li_{13}In_3$ framework with a high surface area can further facilitate a uniform Li deposition. Moreover, during the plating process, the Li-ions tend to deposit in the 3D $Li_{13}In_3$ scaffold selectively and smoothly because of the lithiophilicity of ZnO coating, inducing the formation of a uniform lithium layer covering the surface of the metal alloy framework. Therefore, plated Li atoms can be filled into the interior porosity of the LiRLIA electrode instead of aggregating on the surface during a lithiation/delithiation process, thus avoiding Li dendrite growth.

To clarify the Li plating/stripping behavior of the designed LiRLIA electrode and bare Li, the surface morphology of cathode and anode at different stages of Li symmetric cells is studied by SEM (current density is controlled at 0.5 mA cm^{-2}). Before SEM analysis, both bare Li and LiRLIA symmetric cells are disassembled and then soaked in a DME solution for 12 h to remove the SPEs. When the areal capacity is controlled to 0.2 mAh cm^{-2}, as shown in Figure 3b (anode part during the charging process), Li prefers to deposit and nucleate along with the 3D $Li_{13}In_3$ framework. This deposited Li is totally from the cathode that acts as Li source, which is delithiated and leads to some micropores structure in the cathode (Figure 3c). And when the capacity rises to as high as 0.5 mAh cm^{-2}, and 1 mAh cm^{-2}, the Li deposition is completely uniform with a dense layer, no obvious Li aggregation and dendrites observed (Figure 3d,f). While the Li can be extracted from the LiRLIA cathode, a stable framework is well retained, as shown in Figure 3e,g. A larger microporous structure in the electrode is observed with an increase of capacity. So, the Li-In alloy ($Li_{13}In_3$) can act as a 3D scaffold for Li accommodation and Li dendrite suppression. Moreover, when the cell reverses to the discharge process with a controlled capacity of 1 mAh cm^{-2}, as shown in Figure 3h, the designed LiRLIA anode can almost fully reverse to the original structure. At the cathode, the micropores are mostly filled by lithium that is totally from the anode, as shown in Figure 3i. This means high reversibility of LiRLIA, where Li transports between anode and cathode without structure change during the charging/discharging process. However, a significant difference between the bare Li and LiRLIA electrodes can be seen. For the bare Li anode, some irregular moss-like Li is appeared (Figure S10a,c, Supporting Information). Especially at a high capacity of 1 mAh cm^{-2}, the Li aggregation is obvious (Figure S10e, Supporting Information), accelerating the growth of lithium dendrite which can limit the Li symmetric cell performance. Bare Li cathode also delivers an inhomogeneous and irreversible Li delithiated process. As shown in Figures S10b,d, and S9f, Supporting Information, lots of Li pits can be seen. In addition, after reversing to 1 mAh cm^{-2}, there is a large porous structure inside the Li anode that cannot reverse to the pristine structure (Figure S10g, Supporting Information). Dead Li formation is obvious on the surface of a Li cathode which can decrease the cycle life of bare Li symmetric cell (Figure S10h, Supporting Information). The difference between LiRLIA and bare Li electrode further highlights the advantages of LiRLIA, where $Li_{13}In_3$ framework provides a stable host possessing high surface area and sufficient interior space for guiding uniform deposition of lithium, inhibiting lithium dendrites growth, and dramatic volume changes.

To further demonstrate the unique properties of LiRLIA anode, the electrochemical performance of two different ASSLBs assembled with LiRLIA anode and bare Li anode as counterparts is studied. The design of the ASSLB with LiRLIA anode and LFP cathode can be illustrated in **Figure 4**a, where an SPE is sandwiched between the cathode and anode. For the cathode design, vertically aligned LFP is selected to provide more Li^+ transport channels with reduced Li^+ transport tortuosity compared with conventional blade cast LFP cathode, thus further facilitating Li^+ transport during the full battery cycling.[17] As shown in Figure S11, Supporting Information, the microwalls of the designed LFP cathode (thickness: around 10 μm) and micro-channels (distance: around 20 μm) clearly confirm the vertically aligned structure design. The Li-LFP coin cell constructed with LiRLIA (named as LFP|SPE|LiRLIA) and bare Li (LFP|SPE|Li) as counterpart is first studied under galvanostatic charge/discharge current density of 0.2 C between 2.5 and 4.0 V, where the same SPE in the Li–Li symmetric cells is employed as SSE (Figure 4b). It illustrates that the LFP|SPE|LiRLIA cell has a similar specific capacity compared with the LFP|SPE|Li cell at a low current density of 0.2 C. However, Figure 4c shows that the LiRLIA anode has a lower Li nucleation voltage than that of the bare Li anode, indicating a lower energy barrier of Li stripping/plating with LiRLIA anode in the cells.[14a] Then, the rate performance of two different kinds of cells under different rates from 0.2 to 10 C in the voltage window of 2.5–4.0 V is detected in Figure 4d. As a result, the LFP|SPE|LiRLIA cell presents a better rate performance than that of the LFP|SPE|Li cell. Even at a high rate of 10 C, the cell using LiRLIA anode can still deliver a high specific capacity of around 100 mAh g^{-1}, while the LFP|SPE|Li cell displays a capacity of just ≈60 mAh g^{-1}. The improved rate performance can be attributed to the fast Li^+ transport in the 3D $Li_{13}In_3$ scaffold during the charging/discharging process, thus leading to lower overpotentials.[16a] The overpotential of both different kinds of cells is determined by the voltage difference as shown in Figure 4e and Figure S12, Supporting Information. It delivers a lower overpotential of the designed LiRLIA anode than that of the bare Li anode, also demonstrating the lower energy barrier if designed LiRLIA anode during the charging/discharging process in ASSLBs. At the rate of 10 C, the cell using LiRLIA anode has a low overpotential of 69 mV (Figure 4e), whereas that of the cell assembled with bare Li is 92 mV (Figure S12, Supporting Information). Moreover, to demonstrate the long-term cycle capability of both cells, after the rate performance-tested, the cells assembled with both LiRLIA and bare Li anode are studied at a high rate of 5 C in Figure 4f. Over more than 2000 cycles, the LFP|SPE|LiRLIA cell exhibits virtually no fading and maintains a capacity of 125 mAh g^{-1}; moreover, the cell sustains over 83% retention after 2000 cycles. In comparison, the cell using bare Li as anode

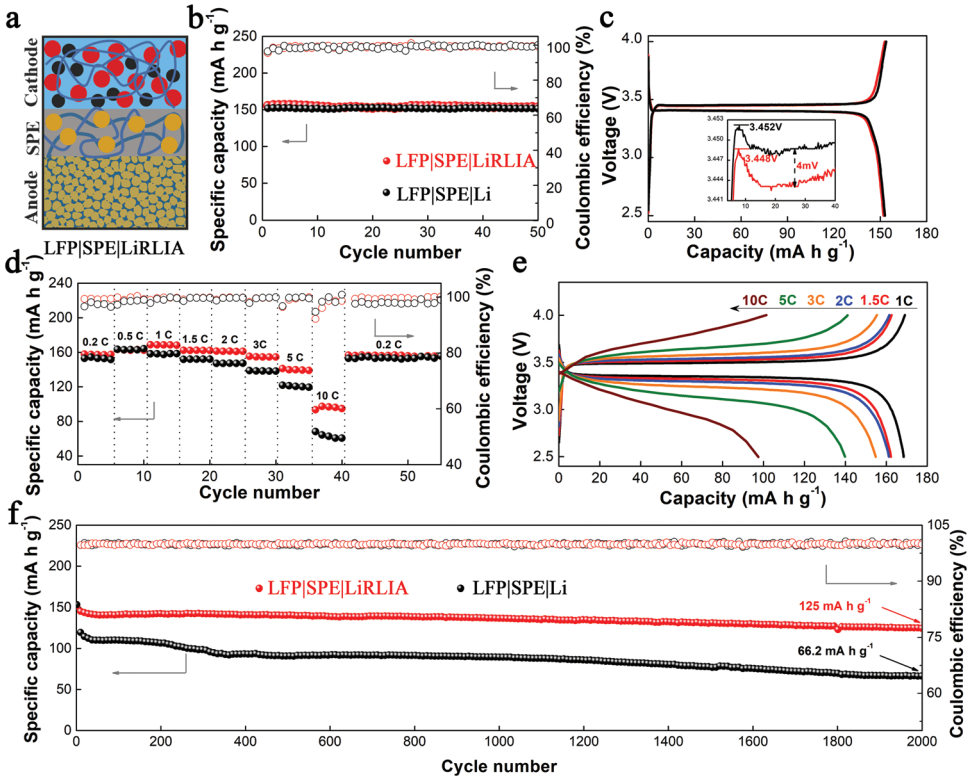

Figure 4. Electrochemical performance of ASSLBs with two different cell configurations (LFP|SPE|LiRLIA, LFP|SPE|Li). a) Schematic illustration of LFP cathode and LiRLIA anode with SPE for ASSLBs. b) The cells of LFP|SPE|LiRLIA and LFP|SPE|Li cycling performance at a rate of 0.2 C. c) Charge and discharge profile of both cells at 0.2 C. d) LFP|SPE|LiRLIA and LFP|SPE|Li full batteries rate performance from 0.2 to 10 C. e) Charge and discharge profile of LFP|SPE|LiRLIA at different rates. f) LFP|SPE|LiRLIA and LFP|SPE|Li full batteries long cycling performance at a rate of 5 C.

shows a much lower capacity and faster capacity decay, which is 66.2 mAh g^{-1} after 2000 cycles. The results further confirm that the proposed LiRLIA electrode with its unique deposition behavior can remarkably increase the cycle life and increase the reversible capacity and rate performance of ASSLBs through enhanced Li^+ transport and dead Li/Li dendrite suppression.

To further verify the experimental results, we calculated adsorption energy and Li atom migration on the surfaces of Li metal and $Li_{13}In_3$ alloy, using the density functional theory (DFT) calculations. The computational details could be found in the experimental section. The most stable Li surface has been demonstrated to be the (100) surface.[18] As for $Li_{13}In_3$ alloy, seven different surfaces were cut (as shown in Figure S13, Supporting Information) and their lattice parameters are summarized in Table S2, Supporting Information. The surface energy of $Li_{13}In_3$ (100), (010), and (001) is calculated to be –1.97 eV (as shown in Figure S14, Supporting Information), indicating that the three surfaces have similar stability. In the subsequent calculations, we select Li (100) and $Li_{13}In_3$ (100) surfaces to calculate the adsorption energy and energy barrier of the Li atom. As shown in **Figure 5**a,b (corresponding with Figure S15a,b, Supporting Information) the top, hollow, and bridge adsorption sites are considered. The Li atom prefers to adsorb on the hollow and bridge sites on the Li (100) surface (as shown in Figure 5c, and Table S3, Supporting Information), despite the slightly different adsorption energies of –1.36 and –1.31 eV, which is consistent with the results reported by Gaissmaier et al.[19] As for the $Li_{13}In_3$ (100) surface, the Li atom is also easier to adsorb on the hollow and bridge sites. The more negative values of adsorption suggest stronger bonding between Li and the substrate, indicating that Li atoms interact stronger over $Li_{13}In_3$ (100) surface than Li (100) surface. It could be used to interpret why Li preferentially deposits on the $Li_{13}In_3$ surface.

Additionally, minimum energy pathways for Li atom over Li (100) and $Li_{13}In_3$ (100) surface are summarized in Figure 5d,e. Figure 5f shows that the Li diffusion energy barrier over Li (100) surface is determined to be 0.48 eV, by taking the energy difference between the initial and transition state, which is comparable with the reported value of 0.47 eV.[20] In the case of the $Li_{13}In_3$ (100) surface, the energy barrier of Li diffusion is determined to be 0.37 eV as displayed in Figure 5f. Following the Arrhenius equation, the diffusion constant was given by

$$D \propto \exp\left(-E_a / k_B T\right) \tag{1}$$

where k_B is the Boltzmann constant, T is the operating temperature, and ν is the prefactor, with the value of the order of 10^{13} Hz. By using the Arrhenius equation we find the diffusion of Li atom on the $Li_{13}In_3$ (100) surface is $\approx 10^2$ times faster than Li (100) surface at 300 K. Based on the DFT calculations, the higher adsorption energy and lower diffusion barrier on the surface of $Li_{13}In_3$ (100) surface results in Li atom selective deposition and fast diffusion on this surface.

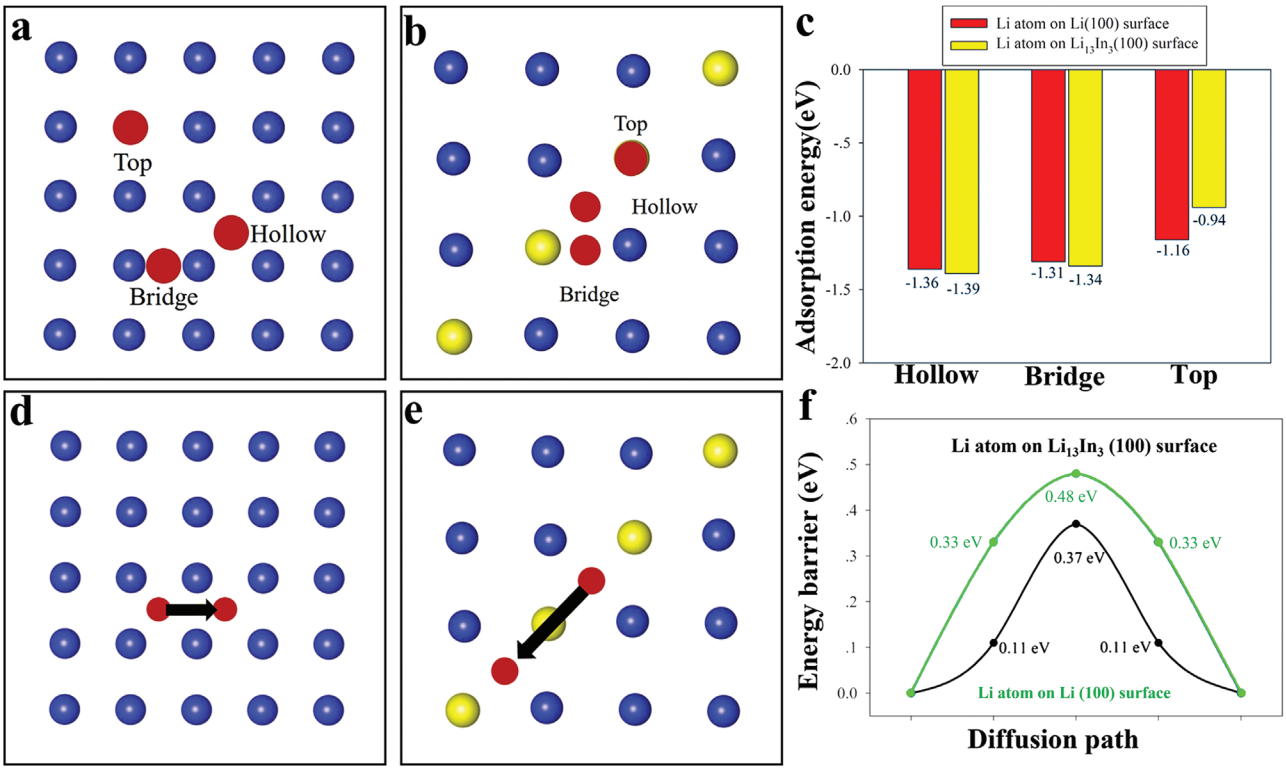

Figure 5. The illustration of a) Li (100) and b) $Li_{13}In_3$ (100) surfaces and possible adsorption sites. The blue and yellow sphere represents the Li and In atom, respectively. The red sphere represents the possible adsorption sites, including the hollow, top, and bridge sites. c) The adsorption energy (eV) of Li atom on Li (100) and $Li_{13}In_3$ (100) surfaces. d,e) The Li diffusion path on the Li (100) and $Li_{13}In_3$ (100) surfaces, respectively. f) Energy barrier on the Li (100) and $Li_{13}In_3$ (100) surfaces.

3. Conclusion

In summary, we designed a LiRLIA electrode with a well-controlled $Li_{13}In_3$ alloy framework filled with Li within to suppress Li dendrite growth for realizing high-energy-density ASSLBs. The $Li_{13}In_3$ alloy framework can guide the selective nucleation and growth of Li on the framework. Furthermore, the residual Li acts as a Li source and transports between the anode and cathode during the charging/discharging process, recovering the Li's potential, ultimately attributing to higher energy density output of ASSLBs. Based on DFT calculation, we find the higher adsorption energy and lower diffusion barrier on the surface of $Li_{13}In_3$ (100) are beneficial for Li atom selective deposition and fast diffusion. Thus, the symmetric cell using the LiRLIA electrode stably runs for over 6800 h at a current density/capacity of 0.5 mA cm^{-2}/1mAh cm^{-2}. Even at high current densities and areal capacities of 5 mA cm^{-2} and 5 mAh cm^{-2}, the symmetric cell can still run about 1000 h without overpotential decay, which is over one of magnitude higher than most previous SPE-based cells. The strong Li dendrite resistance of the LiRLIA anode enables the LFP|SPE|LiRLIA full cell with excellent rate capability and cycling performance. The cell with LiRLIA anode shows an excellent rate performance, even at a high rate of 10 C, delivering a high specific capacity of around 100 mAh g^{-1}. Moreover, when the cell cycles at a high rate of 5 C, it maintains a high discharge capacity of 125 mAh g^{-1} after 2000 cycles, which demonstrates a long cycle life capability. This result indicates that this work provides important guidance for the realization of high-energy-density and high-power-density ASSLBs by using a Li-metal alloy anode.

4. Experimental Section

Synthesis of CNT@ZnO Template: CNTs coated with a conformal layer of ZnO were fabricated by using ALD with the use of the Gemstar-8 ALD system (Arradiance, USA) with diethyl zinc (DEZn) and DI water as precursors. 100 ms pulses of DEZn and DI water were alternated with 30 s purge times in between each sub-cycle. Afterward, the CNT@ZnO template was obtained using a custom-made 3D printer equipped with a 3-axis micro-positioning stage (Fisnar 4200N printer). Typically, CNT@ZnO and sodium alginate were mixed at a weight ratio of 9:1 with additional DI water to prepare the printing ink. After mixing, the ink was loaded into a 3-mL syringe and extruded through a 400-µm-diameter nozzle. Then the CNT@ZnO ink was printed into a dense structure with an overall diameter of 10 mm at a print motion speed of 6 mm s^{-1} with a pressure of 70 dpi. Finally, the printed CNT@ZnO was dried using a freeze-dryer at −50 °C for 20 h to get a vertically aligned CNT@ZnO template.

Synthesis of Li-Rich $Li_{13}In_3$ Alloy Electrode: Infusion of molten LiRLIA was carried out in an Ar-filled glovebox. Typically, Li foil (99.9%, Alfa Aesar) and In foil (99.9%, Alfa Aesar) were put into a stainless-steel crucible and heated to ≈350 °C on a hot plate (VWR), and a spontaneous reaction between metallic lithium and In to realize a Li-rich LiIn alloy (LiRLIA). Subsequently, the edge of the printed CNT@ZnO template was put into contact with the molten LiRLIA. The LiRLIA would then

steadily climb the scaffold and wet the whole matrix, forming the 3D LiRLIA electrode.

Synthesis of VA-LFP Cathode: For the VA-LFP cathode, the 3D vertically-aligned LFP cathode, named VA-LFP, was obtained by the 3D printing technique combined with the freeze-drying method. Typically, the LFP powders, C_{65}, conductive carbon, and PEO-PEGDME/LITFSI (EO/Li = 12/1 and PEO (Mw:1000000)/PEGDME = 1:1) were dissolved in water with a weight ratio of 7:1:2 to form a slurry. And then the ink was loaded into a 3-mL syringe and extruded through a nozzle. The LFP ink was printed into a dense structure with an overall diameter of 10 mm at a print motion speed of 8 mm s^{-1} with a pressure of 70 dpi. Subsequently, the printed cathode was dried using freeze-drying at −50 °C for 20 h to fabricate a VA-LFP cathode. The active material loading for VA- LFP was around 2.5 mg cm^{-2}.

Preparation of Solid-Polymer Electrolytes: The poly(ethylene glycol) dimethyl ether (PEGDME) based SPEs were prepared using a solution-free method. Typically, a mixture of PEGDME and Li-salts (lithium (trifluoromethylsulfonyl) imide (LiTFSI) and lithium bis(fluorosulfonyl) imide (LiFSI)) weight ratio of 60:4:1 was directly heated to 120 °C and held at that temperature until the polymers were completely melted and salts were dissolved. Moreover, in order to confirm the thickness of SPEs, a battery that runs at 60 °C was disassembled and then the cellulose separator was chosen to remove the surface liquid. After testing by spiral micrometer, the total thickness of the SPEs including the cellulose membrane was around 50 µm. Therefore, the specified thickness of the SPEs was around 25 µm due to the 25 µm thickness of pure cellulose membrane. All the aforementioned processes were conducted in an Ar-filled glove box.

Characterizations: Hitachi S-4800 field-emission scanning electron microscope equipped with energy dispersive spectroscopy was used to characterize the morphologies of the electrodes.

Electrochemical Measurements: All electrochemical performances of the solid-state full cells and Li–Li symmetrical cells were tested with CR2032 coin cells, constructed in an Ar-filled glove box. The cathode (VA-LFP) and Li anode (bare Li and LiRLIA), Li symmetrical cells, and LiRLIA symmetric cells were separated by a cellulose membrane. During the cell assembly, the SPE should be first heated to 120 °C to keep the liquid state of the electrolyte. And then the cellulose membrane was infused into SPE to confirm the excellent wetting capability of the separator. After that, the cathode and anode parts can be put and assembled as a full battery. Discharge tests were carried out using a LAND CT-2001A system, by applying different current densities.

To measure the electrochemical performance of the electrodes, Li–Li symmetric cells employed with bare Li and LiRLIA were tested under different current densities. For the full cell testing, the LFP was employed as the cathode with an active material loading of about 2.5 mg cm^{-2}, bare Li, and LiRLIA as an anode, labeled as LFP|SPE|Li, LFP|SPE|LiRLIA, respectively. The charge–discharge testing of the full-cell batteries were carried out using a LAND CT-2001A system within a voltage range of 2.5–4.0 V at 60 °C. Unless otherwise specified, the specific capacities reported in this work were calculated based on LFP and the voltages concerning Li^+/Li.

Computational Details: All calculations were carried out within the DFT framework as implemented in Vienna ab initio simulation package. The projector augmented-wave pseudopotentials were used to describe the interaction between ions and electrons, and the exchange-correlation effects were treated using the Perdew–Burke–Ernzerhof functional under the generalized gradient approximation.[21] Herein, the electronic configurations for the PAW potentials were $1s^2 2s^1$ for Li and $5s^2 5p^1$ for In.

The unit cell of Li and $Li_{13}In_3$ was optimized using a 4 × 4 × 4 Monkhorst–Pack grid of k-points and the kinetic energy cutoffs of 450 eV were used. It is noted that the Li (100) surface is the most stable surface.[18] As for $Li_{13}In_3$ alloy, 7 surfaces were considered, as shown in Figure S14, Supporting Information. The surface energies were calculated using the following expression,

$$E_{surf} = (E_{slab} - nE_{bulk})/2S \quad (2)$$

where E_{surf} is the surface energy, E_{slab} is the energy of the slab containing n units of $Li_{13}In_3$, E_{bulk} is the bulk energy per unit, and S is the area of the surface. The dispersion corrections arising from van der Waals forces were calculated using the DFT-D3 approach.[22] The vacuum space in the z-direction was about 10 Å to avoid the interaction between neighboring. The supercell of Li (100) and $Li_{13}In_3$ (100) surface consist of 180 and 128 atoms, respectively. On the other hand, for optimizing the supercells of Li (100) and $Li_{13}In_3$ (100) surfaces, a 4 × 4 × 1 Monkhorst–Pack grid of k-points was used. The VESTA package was used to visualize the various bulk and surface structures.[23]

For adsorption energy calculations, a Li atom was placed at 3 Å away from the 2D surface. Three adsorption sites including bridge, hollow and top were considered, as shown in Figure 5a,b. The adsorption energy of a Li atom adsorbed onto each substrate was calculated using the following expression

$$E_{Ad} = E_{substrate+Li} - E_{substrate} - E_{Li} \quad (3)$$

where $E_{substrate+Li}$ is the total energy of a Li atoms bound to the 2D surface, $E_{substrate}$ is the energy of the substrate, and E_{Li} is the energy per Li atom in bulk. A positive value of E_{Ad} would suggest desorption, whereas a more negative and would suggest stronger chemical interaction.[24] Minimum energy path profiles were computed using the climbing image nudged elastic band[19] method for simulating the diffusion of a Li atom over both Li (100) and $Li_{13}In_3$ (100) surfaces. All the atoms of hybrid heterostructures were optimized until the total energies converged to below 10^{-4} eV and the forces acting on atoms were less than 10^{-3} eV $Å^{-1}$.

Supporting Information

Supporting Information is available from the Wiley Online Library or from the author.

Acknowledgements

This research was supported by the Natural Science and Engineering Research Council of Canada (NSERC), the Canada Research Chair Program (CRC), the Canada Foundation for Innovation (CFI), and Western University. The authors gratefully acknowledge the financial support from the National Natural Science Foundation of China (22208039) and Basic Scientific Research Project of Educational Department of Liaoning Province (LJKMZ20220878).

Conflict of Interest

The authors declare no conflict of interest.

Author Contributions

X.G., X.Y., and M.J. contributed equally to this work. They conceived the idea and designed the experiments. X.S., C.V.S. and J.W. as supervisors gave guidance and discussion to the project. M.Z. helped with the scanning electron microscope (SEM) test. Y.Z. discussed the experiments. R.L. assisted with characterizations. W.R., H.H., and R.S. gave some comments on this manuscript writing. All authors discussed the results and commented on the manuscript.

Data Availability Statement

Research data are not shared.

Keywords

density functional theory calculation, High-energy-density solid-state batteries, Li dendrite suppression, Li-rich $Li_{13}In_3$ alloy, Li's potential level

Received: August 22, 2022
Revised: October 31, 2022
Published online:

[1] a) Y.-K. Sun, *ACS Energy Lett.* **2020**, *5*, 3221; b) Y.-G. Lee, S. Fujiki, C. Jung, N. Suzuki, N. Yashiro, R. Omoda, D.-S. Ko, T. Shiratsuchi, T. Sugimoto, S. Ryu, J. H. Ku, T. Watanabe, Y. Park, Y. Aihara, D. Im, I. T. Han, *Nat. Energy* **2020**, *5*, 299; c) K. B. Hatzell, X. C. Chen, C. L. Cobb, N. P. Dasgupta, M. B. Dixit, L. E. Marbella, M. T. McDowell, P. P. Mukherjee, A. Verma, V. Viswanathan, A. S. Westover, W. G. Zeier, *ACS Energy Lett.* **2020**, *5*, 922; d) J. Wu, L. Shen, Z. Zhang, G. Liu, Z. Wang, D. Zhou, H. Wan, X. Xu, X. Yao, *Electrochem. Energy Rev.* **2021**, *4*, 101; e) X. Gao, M. Zheng, X. Yang, R. Sun, J. Zhang, X. Sun, *Mater. Today* **2022**, *59*, 161.

[2] a) N. Kamaya, K. Homma, Y. Yamakawa, M. Hirayama, R. Kanno, M. Yonemura, T. Kamiyama, Y. Kato, S. Hama, K. Kawamoto, A. Mitsui, *Nat. Mater.* **2011**, *10*, 682; b) Y. Pang, J. Pan, J. Yang, S. Zheng, C. Wang, *Electrochem. Energy Rev.* **2021**, *4*, 169; c) C. Wang, T. Deng, X. Fan, M. Zheng, R. Yu, Q. Lu, H. Duan, H. Huang, C. Wang, X. Sun, *Joule* **2022**, *6*, 1770.

[3] a) P. Hu, Y. Duan, D. Hu, B. Qin, J. Zhang, Q. Wang, Z. Liu, G. Cui, L. Chen, *ACS Appl. Mater. Interfaces* **2015**, *7*, 4720; b) H. Xu, H. Zhang, J. Ma, G. Xu, T. Dong, J. Chen, G. Cui, *ACS Energy Lett.* **2019**, *4*, 2871; c) Q. Zhou, J. Ma, S. Dong, X. Li, G. Cui, *Adv. Mater.* **2019**, *31*, 1902029; d) X. Yang, M. Jiang, X. Gao, D. Bao, Q. Sun, N. Holmes, H. Duan, S. Mukherjee, K. Adair, C. Zhao, *Energy Environ. Sci.* **2020**, *13*, 1318.

[4] a) H. Liu, X.-B. Cheng, J.-Q. Huang, H. Yuan, Y. Lu, C. Yan, G.-L. Zhu, R. Xu, C.-Z. Zhao, L.-P. Hou, C. He, S. Kaskel, Q. Zhang, *ACS Energy Lett.* **2020**, *5*, 833; b) X. Yang, Q. Sun, C. Zhao, X. Gao, K. R. Adair, Y. Liu, J. Luo, X. Lin, J. Liang, H. Huang, *Nano Energy* **2019**, *61*, 567; c) G. G. Eshetu, X. Judez, C. Li, O. Bondarchuk, L. M. Rodriguez-Martinez, H. Zhang, M. Armand, *Angew. Chem., Int. Ed.* **2017**, *56*, 15368.

[5] A. Banerjee, X. Wang, C. Fang, E. A. Wu, Y. S. Meng, *Chem. Rev.* **2020**, *120*, 6878.

[6] P. Yao, H. Yu, Z. Ding, Y. Liu, J. Lu, M. Lavorgna, J. Wu, X. Liu, *Front. Chem.* **2019**, *7*, 00522.

[7] V. P. H. Huy, S. So, J. Hur, *Nanomaterials* **2021**, *11*, 614.

[8] C. Xin, K. Wen, S. Guan, C. Xue, X. Wu, X. Wu, L. Li, C.-W. Nan, *Front. Mater.* **2022**, *9*, 864478.

[9] L. Li, H. Dai, C. Wang, *Nano Select.* **2021**, *2*, 16.

[10] H. Huo, J. Liang, N. Zhao, X. Li, X. Lin, Y. Zhao, K. Adair, R. Li, X. Guo, X. Sun, *ACS Energy Lett.* **2020**, *5*, 2156.

[11] X. Yang, Q. Sun, C. Zhao, X. Gao, K. Adair, Y. Zhao, J. Luo, X. Lin, J. Liang, H. Huang, L. Zhang, S. Lu, R. Li, X. Sun, *Energy Storage Mater.* **2019**, *22*, 194.

[12] a) Z. Cai, Y. Ou, B. Zhang, J. Wang, L. Fu, M. Wan, G. Li, W. Wang, L. Wang, J. Jiang, Z. W. Seh, E. Hu, X.-Q. Yang, Y. Cui, Y. Sun, *J. Am. Chem. Soc.* **2021**, *143*, 3143; b) J. Zhang, J. Yang, T. Dong, M. Zhang, J. Chai, S. Dong, T. Wu, X. Zhou, G. Cui, *Small* **2018**, *14*, 1800821.

[13] a) S. Y. Han, J. A. Lewis, P. P. Shetty, J. Tippens, D. Yeh, T. S. Marchese, M. T. McDowell, *Chem. Mater.* **2020**, *32*, 2461; b) J. Qu, J. Xiao, T. Wang, D. Legut, Q. Zhang, *J. Phys. Chem. C* **2020**, *124*, 24644; c) M. Wan, S. Kang, L. Wang, H.-W. Lee, G. W. Zheng, Y. Cui, Y. Sun, *Nat. Commun.* **2020**, *11*, 829; d) Z. Tu, S. Choudhury, M. J. Zachman, S. Wei, K. Zhang, L. F. Kourkoutis, L. A. Archer, *Nat. Energy* **2018**, *3*, 310.

[14] a) S. Liu, Y. Ma, Z. Zhou, S. Lou, H. Huo, P. Zuo, J. Wang, C. Du, G. Yin, Y. Gao, *Energy Storage Mater.* **2020**, *33*, 423; b) X. Wu, W. Zhang, N. Wu, S.-S. Pang, Y. Ding, G. He, *Adv. Energy. Mater.* **2021**, *11*, 2003082.

[15] a) X. Gao, X. Yang, Q. Sun, J. Luo, J. Liang, W. Li, J. Wang, S. Wang, M. Li, R. Li, T.-K. Sham, X. Sun, *Energy Storage Mater.* **2020**, *24*, 682; b) S. Deville, *Adv. Eng. Mater.* **2008**, *10*, 155.

[16] a) X. Gao, X. Yang, K. Adair, X. Li, J. Liang, Q. Sun, Y. Zhao, R. Li, T.-K. Sham, X. Sun, *Adv. Energy Mater.* **2020**, *10*, 1903753; b) E. C. Dandley, A. J. Taylor, K. S. Duke, M. D. Ihrie, K. A. Shipkowski, G. N. Parsons, J. C. Bonner, *Part. Fibre Toxicol.* **2017**, *14*, 26; c) M. Staszuk, D. Pakuła, L. Reimann, M. Król, M. Basiaga, D. Mysłek, A. Kříž, *Mater.* **2020**, *13*, 4223.

[17] X. Gao, X. Yang, K. Adair, J. Liang, Q. Sun, Y. Zhao, R. Li, T.-K. Sham, X. Sun, *Adv. Funct. Mater.* **2020**, *30*, 2005357.

[18] D. Gaissmaier, D. Fantauzzi, T. Jacob, *J. Chem. Phys.* **2019**, *150*, 041723.

[19] G. Henkelman, B. P. Uberuaga, H. Jónsson, *J. Chem. Phys.* **2000**, *113*, 9901.

[20] S. Liu, Q. Zhao, X. Zhang, J. Liu, L. Dai, L. Wang, J. Luo, *J. Mater. Chem. A* **2020**, *8*, 174115.

[21] J. P. Perdew, K. Burke, M. Ernzerhof, *Phys. Rev. Lett.* **1996**, *77*, 3865.

[22] S. Grimme, *J. Comput. Chem.* **2006**, *27*, 1787.

[23] K. Momma, F. Izumi, *J. Appl. Crystallogr.* **2008**, *41*, 653.

[24] X. Yang, M. Jiang, X. Gao, D. Bao, Q. Sun, N. Holmes, H. Duan, S. Mukherjee, K. Adair, C. Zhao, J. Liang, W. Li, J. Li, Y. Liu, H. Huang, L. Zhang, S. Lu, Q. Lu, R. Li, C. V. Singh, X. Sun, *Energy Environ. Sci.* **2020**, *13*, 1318.